Quaternary Science Reviews 310 (2023) 108128

Contents lists available at ScienceDirect

Quaternary Science Reviews

journal homepage: www.elsevier.com/locate/quascirev

Precession and obliquity forcing of the South African monsoon revealed by sub-tropical fires

Anne-Laure Daniau [a, *], Marie-France Loutre [b, c], Didier Swingedouw [a], Thomas Laepple [d, e], Franck Bassinot [f], Bruno Malaizé [a], Masa Kageyama [f], Karine Charlier [a], Hervé Carfantan [g]

[a] University Bordeaux, CNRS, Bordeaux INP, EPOC, UMR 5805, F-33600 Pessac, France
[b] Université Catholique de Louvain, Belgium
[c] Past Global Changes (PAGES), Bern, Switzerland
[d] Alfred-Wegener-Institut, Helmholtz-Zentrum for Polar and Marine Research, Potsdam, Germany
[e] University of Bremen, MARUM – Center for Marine Environmental Sciences and Faculty of Geosciences, 28334, Bremen, Germany
[f] Laboratoire des Sciences Du Climat et de L'Environnement, LSCE/IPSL, CEA-CNRS-UVSQ Université Paris-Saclay, Gif-sur-Yvette, France
[g] Institut de Recherche en Astrophysique et Planétologie (IRAP), Observatoire Midi-Pyrénées Site Belin, Toulouse, France

ARTICLE INFO

Article history:
Received 3 February 2023
Received in revised form
10 May 2023
Accepted 10 May 2023
Available online xxx

Handling Editor: P Rioual

Keywords:
Fire
Biomass burning
Heterodynes
Monsoon
Linear and non-linear response
Marine sediment

ABSTRACT

While the influence of precession on monsoon at low latitudes through insolation forcing is well-known, the role of obliquity is still debated since its influence on the distribution of incoming solar radiation is small in these regions. In southern Africa, long marine and terrestrial sedimentary records attest of a precessional influence on the South African monsoon at orbital time scale. The obliquity signal is occasionally observed in the geological records although modeling results suggest an influence of precession and obliquity on summer monsoon. Here, we present a record of microscopic charcoal from core MD96-2098 located off Namibia covering the past 184,000 years. Our record of fire activity reveals cyclic changes at frequencies of 23, 58 and 12 kyr^{-1} and lacks the obliquity signal at 41 kyr^{-1}. Changes in fire over southern Africa are interpreted as shifts in large and intense fires spreading in open-grassland savanna as a result of orbitally-driven changes in rainfall intensity associated with the South African monsoon. We show that, despite the absence of a 41 kyr obliquity imprint, the presence of 23, 58 and 12 kyr^{-1} frequencies likely stems from a nonlinear response of fire to precipitation controlled by a combination of precession and obliquity frequencies, supporting the influence of obliquity on the South African monsoon.

1. Introduction

Changes in the orbital precession parameter result in an antiphase evolution of the summer insolation between hemispheres (Berger, 1978a), which leads to an enhancement of southern (northern) monsoon precipitation during austral (boreal) summer insolation maxima (Kutzbach et al., 2008). Such an antiphase relationship is supported by spectral response of several palaeoclimate records with variance concentrated within the precession-band cyclicity of 23 kyr (with 1 kyr = 1000 years), such as the South American and Asian monsoons deduced from speleothem archives (Cheng et al., 2012; Cruz et al., 2005; Wang et al., 2008), the North African monsoon reconstructed by marine fossil fauna assemblage variations (McIntyre et al., 1989), by sapropels (Rossignol-Strick, 1985) or by dust fluxes (Crocker et al., 2022; deMenocal, 1995; Skonieczny et al., 2019; Tiedemann et al., 1994).

Changes in southern African climate at precessional frequencies are rarely documented by long palaeoclimate records on land due to their poor preservation. The 200,000 year-long Tswaing crater's record located in southern Africa at 26°S was the first one showing rainfall peaks during austral summer insolation maxima (Partridge, 1997; Partridge et al., 1997). Speleothem records of oxygen and carbon stable isotope ratios from the Greater Cape Floristic Region suggest increases in summer rainfall and a wider spread of C_4 grasses associated with precession maxima in the Greater Cape

* Corresponding author.
E-mail address: anne-laure.daniau@u-bordeaux.fr (A.-L. Daniau).

https://doi.org/10.1016/j.quascirev.2023.108128

Floristic Region (Braun et al., 2018) although the influence of low latitude direct insolation forcing appears to be supplanted by high latitude forcing from 70 ka onwards (Chase et al., 2021) (with 1 ka = 1000 years before present). More recently, periods of speleothem growth during summer insolation maxima were reported in Madagascar (Burns et al., 2022). This cyclicity in the precession band is also observed in several long marine sedimentary records off southern Africa that contain proxies of environmental shifts on land, i.e. changes in abundance of C_4 grasses of southwestern Africa (Collins et al., 2014), in palaeofire activity of southern Africa (Daniau et al., 2013), in river-discharge (Caley et al., 2018; Simon et al., 2015) and in lowland forest development of southeastern Africa (Dupont, 2011), and in fynbos elements in the Greater Cape Floristic Region (Dupont et al., 2022).

Those palaeoclimate records support the concept of a global monsoon which ties together six monsoon regions, including the South African monsoon, defined on the basis of precipitation-related characteristics (Wang, 2009). The global link between regional monsoons results from north-south movements of the Intertropical Convergence Zone (ITCZ) at orbital time scale (Wang et al., 2014, 2017). However, this concept has been questioned since regional differences in the timing of the monsoon response to orbital forcing were reported in Indian, East Asian, West African and East African monsoon sectors, as well as differences in the weight of precession and obliquity in the monsoon records (Caley et al., 2011b). Several studies (Caley et al., 2011c; Clemens and Prell, 1990, 2003) suggest that the response to obliquity forcing (41 kyr cyclicity) observed in Arabian Sea records of summer monsoon is larger than the response to precession forcing (23 kyr cyclicity) although the influence of obliquity on low-latitude insolation is weaker. Modeling results suggest that the North and South African summer monsoons are influenced by both precession and obliquity (Bosmans et al., 2015a; Ding et al., 2021; Tuenter et al., 2003). Evidence of obliquity-related cyclicity is found on land in the southeastern Africa record of mountainous forest (*Podocarpus* pollen) (Dupont, 2011), in fynbos elements of the Cape region (Restionaceae and Stoebe−Elytropappus type) (Dupont et al., 2022) and in the log-transformed pollen concentration of a marine record off Namibia (Urrego et al., 2015). A 41 kyr cyclicity is also observed in the spectral response of the Sea Surface Temperature and Sea Surface Salinity off the Limpopo River in the Indian Ocean (Caley et al., 2011a). These elements clearly suggest that the long-term evolution of the monsoon is not only a precession-story, and that the respective role of precession or precession plus obliquity in the orbital forcing of monsoon still needs to be understood (Wang, 2009).

To address this issue, we present here a 184,000 year-long marine sedimentary record of fire activity obtained from microscopic charcoal particles preserved in deep-sea sediments off Namibia (Fig. 1) resulting from increasing the length and sampling resolution of a previously published record (Daniau et al., 2013). Charcoal is an amorphous inorganic carbon compound resulting from the incomplete combustion of plant elements during fires at temperature ranging between 200 and 600 °C (Jones et al., 1997; Patterson et al., 1987). Microcharcoal particles (charcoal of microscopic size with length >10 and <100 μm) (Whitlock and Larsen, 2001) belong to the fine grained-size sediment fraction transported by wind and water from its source to the sedimentation basin where it is preserved (Patterson et al., 1987). At regional scale, modeling study showed that windborne microcharcoals are deposited within the hydrographic basin in which they are produced (Haliuc et al., 2023) before being transported to the ocean by the fluvial system. Microcharcoal preserved in marine sediments off Namibia likely comes from the large Orange River's catchment area in southern Africa and provides a regional record of fires on southern Africa (Daniau et al., 2013). With the exception of the fynbos region in the Western Cape, fires in southern Africa are largely grass-fueled surface fires mainly controlled by the previous two years of rainfall which drives fuel loads, as well as by a marked rainfall seasonality (Archibald et al., 2010). Thus, we use this fire record as an indirect proxy of rainfall. Our palaeo-fire record was reconstructed from charcoal retrieved in the sediment core MD96-2098 (Bertrand, 1996), located at 2909 m water depth off Namibia (25°35′S, 12°38′E) in the south-eastern Atlantic Ocean (Fig. 1). In order to identify what controls the rainfall and climate of southern Africa and thus better understand sub-tropical monsoon variability over the past 184,000 years, we compared our fire-derived rainfall record with precipitation variability from other subtropical regions, with model-derived climate conditions at key interglacial periods and at the Last Glacial Maximum (LGM), and with orbital parameters.

2. Materials and methods

2.1. Chronostratigraphy of core MD96-2098

The age model of the last 45,000 years is based on fourteen published ^{14}C AMS (accelerator mass spectrometry) dates on single species of planktonic foraminifera when possible (Daniau et al., 2013; Urrego et al., 2015) (Table S1). ^{14}C AMS were calibrated according to the Calib REV8.2 radiocarbon calibration program (Stuiver and Reimer, 1993) (CALIB 8.2 at http://calib.org, accessed 2021-12-1) using the MARINE20 calibration curve (Heaton et al., 2020) and a local reservoir correction, ΔR of −29 ± 18 years calculated as the mean of reservoir age corrections obtained at the three nearest sites (ΔR for the MD96-2098 core location is available at http://calib.org/marine/).

The chronostratigraphy for the older part of MD96-2098 record is based on benthic foraminifera stable $\delta^{18}O$ record. We used the published $\delta^{18}O$ benthic foraminifera record obtained on the *Planulina wullerstorfi* species (corresponding to *Cibicidoides wuellerstorfi* in Pichevin et al. (2005)) and a new $\delta^{18}O$ record of benthic foraminifera *Melonis barleanum* covering the Marine Isotopic Stage 4 (MIS4; this study) (Table S1 and Fig. S1). Oxygen isotopic measurements were preferentially made on benthic foraminifera *P. wullerstorfi* or *Uvigerina*, which are two species commonly used for isotopic stratigraphy. As these species are rare during MIS 4 in marine core MD96-2098, seventy-six stable isotopic analyses were made on *M. barleanum* at the UMR 5805 EPOC - University of Bordeaux, using a *Micromass MultiPrep-Optima isotope ratio* mass spectrometer of the "Plateforme Isotopie". For each measurement, 80 μg mean weight aliquots (4−6 specimens for the benthic species) underwent an individual acid attack to produce CO_2 gas. This gas was analysed versus a laboratory reference gas calibrated with respect to PDB, using the international standard NBS 19. Standard deviations of multiple replicate measurements of this standard are ±0.039‰ (1σ). Previous studies have shown a constant difference between *M. barleanum* and *P. wullerstorfi* of +0.4‰ (Gouzy et al., 2004; Graham et al., 1981) allowing the confirmation of control points published in Daniau et al. (2013) and Urrego et al. (2015) or the better identification of MIS 4.23.

Based on these benthic $\delta^{18}O$ data, the age model for the older part of core MD96-2098 was constructed by identifying marine isotopic events and visually correlating 15 control points to the benthic reference record of Lisiecki and Raymo (2005). Ages were derived from Lisiecki and Raymo (2005) and from additional sources such as speleothems and sea level high stand (Drysdale et al., 2007; Henderson and Slowey, 2000; Masson-Delmotte et al., 2010; Sanchez Goñi and Harrison, 2010; Waelbroeck et al., 2008) (Table S1).

The final age model over the complete MD96-2098 record was

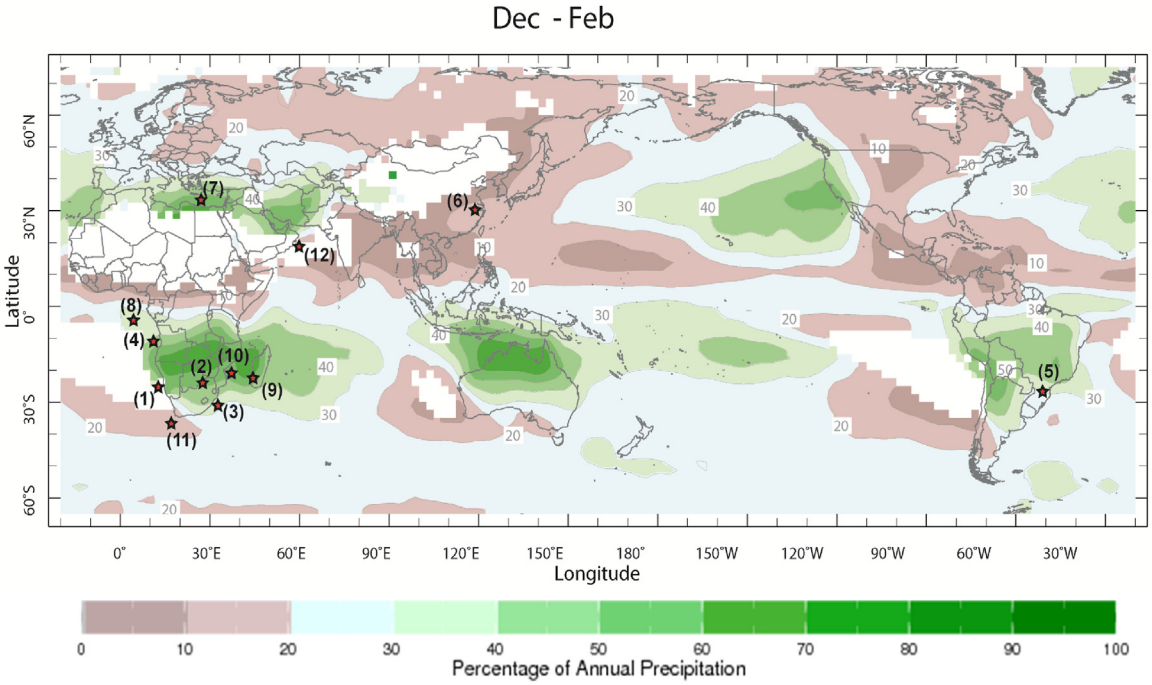

Fig. 1. Location of the records discussed in the text. Percentage of annual precipitation that occurs during December–February (DJF), based upon climatological precipitation using the 1991–2020 CE base period from the monthly CPC Merged Analysis of Precipitation (CMAP) dataset (https://iridl.ldeo.columbia.edu/maproom/Global/Climatologies/?Set-Language=en). Contours are drawn at intervals of 10%. Regions shaded in green receive more than 30% of their annual precipitation, while areas shaded in brown receive less than 20% of their annual precipitation during DJF. 1. Core MD96-2098 (this study); 2. Tswaing Crater record (Partridge et al., 1997); 3. core CD154-10–06 P (Simon et al., 2015); 4. Core MD08-3167 (Collins et al., 2014); 5. Botuvera Cave (Cruz et al., 2005); 6. Sanbao $\delta^{18}O$ records (Wang et al., 2008); 7. Core RC9-181 (Rossignol-Strick, 1985); 8. RC24-16 (McIntyre et al., 1989); 9. Speleothem growth (Burns et al., 2022); 10. Core MD96-2048 (Caley et al., 2018; Dupont et al., 2011); 11. IODP U1479 (Dupont et al., 2022); 12. Arabian sea records (Caley et al., 2011c; Clemens and Prell, 1990, 2003).

then obtained using the age-modeling approach from Blaauw (2010) (CLAM package 2.4.0; implemented in R version 4. 1.2; RStudio, 2021.09.1) with a smooth spline of 0.3. The ages of the upper 22 cm of the core were estimated by extrapolating the depth-age linear regression equation obtained on the ^{14}C-dated portion of the core (using the upper 60 cm of the core). Based on this extrapolation approach, the age of the top 1 cm sample is estimated to be of 647 years cal BP.

2.2. Microcharcoal sampling and analysis

A previous study of microcharcoal (157 samples) based on samples obtained from 6 to 18 m in core MD96-2098 allowed to reconstruct fire activity over the time interval 167–35 ka (Daniau et al., 2013). Here, another set of 265 samples was analysed. Combined with our previously published data, the final dataset continuously covers the sedimentary record of MD96-2098 from 0 to 19.45 m with a mean sampling resolution of 4 cm. This dataset provides a record of changes in biomass burning over the past 184,000 years, including the last climatic cycle and the upper part of MIS 6. The temporal resolution is of about 435 years on average.

Microcharcoal particles were extracted following the protocol presented in Daniau et al. (2013) which consists on successive chemical treatments on ~0.2 g of dried bulk sediment of HCl, HNO_3, H_2O_2 and HF to remove calcium carbonates, organic matter and siliceous materials. Twenty-five samples from MIS 6 containing for some of them high amount of organic matter were processed using hot nitric acid for 1 h. After filtering, the residue was mounted on onto a Poly (methyl methacrylate) (PMMA) slide before gentle polishing for observation under the microscope. Microcharcoal was identified using petrographic criteria under reflected light and counted under transmitted light at x500 magnification using image analysis with a Leica DM6000M microscope. Only particles more than 10 μm in length were included in the analysis (Mooney and Tinner, 2011).

Microcharcoal concentration was expressed in number of fragments per gram of dry bulk sediment (CCnb). As potential fragmentation might occur during chemical processes (Tsakiridou et al., 2020) or during taphonomic processes (Leys et al., 2013), we used also the concentration expressed as total surface area of microcharcoal per gram of dry bulk sediment (CCsurf) to compare with CCnb (Fig. S2). Microcharcoal influx (number of microcharcoal. cm^{-2}. yr^{-1}) was estimated using the wet bulk density because the dry bulk density was not available for core MD96-2098. However, this should not unduly influence the estimates, because the wet and dry bulk densities are linearly correlated in the area, as seen for example in core GeoB1711-4 off the Namib desert (Müller, 2003). Morphological analyses included measurements of the length and width of the black particles to calculate the elongation of microcharcoal, i.e. the length to width ratio. Different elongation ratio criteria based on the literature were used to identify the burnt vegetation type (Fig. 2). A threshold >2.1 on the mean elongation ratio derived from marine archives was set to identify microcharcoal produced by the burning of graminoid-mixed/shrub vegetation corresponding to open grassland-savanna (Haliuc et al., 2023). A mean width to length ratio less than 0.5 derived from terrestrial archives was used to identifying the burning of grassland-dominated vegetation *versus* >0.5 for ligneous vegetation (including both shrubs and trees) (Aleman et al., 2013; Leys et al., 2015). In addition, we used the mean elongation ratios obtained from a synthesis of different experimental analyses conducted on different fuel types (Vachula et al., 2021). In this case, each individual microcharcoal particle was classified as burnt trees and (sub)shrubs using an elongation of <2.5, as burnt shrub/

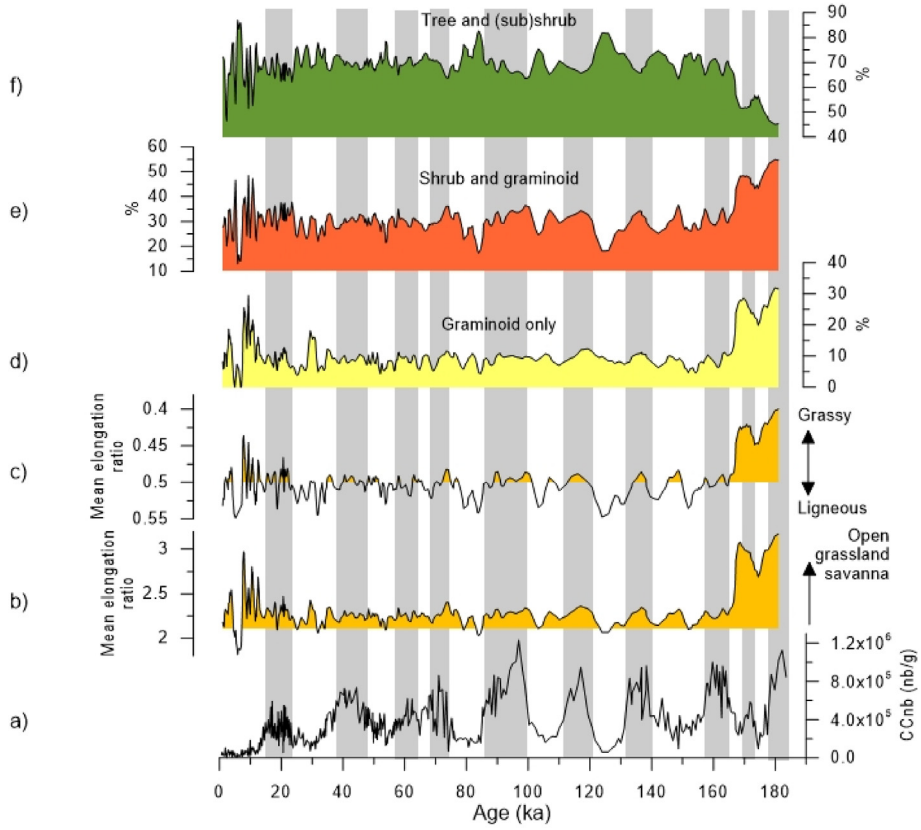

Fig. 2. Microscopic charcoal particles retrieved in core MD96-2098 classified in different burned group based on morphology criteria following Haliuc et al. (2023), Aleman et al. (2013), Leys et al. (2015a) and Vachula et al. (2021). a) Microcharcoal concentration (CCnb) of core MD96-2098; b) Mean charcoal elongation value of core MD96-2098. Orange colour indicates values above 2.2 following the median value of Haliuc et al. (2023) to identify charcoal produced by open-grassland savanna fires versus dwarf open shrubland with scattered trees fires; c) Mean charcoal elongation value of core MD96-2098. Orange colour indicates a width/length ratio of <0.5 used to identify charcoal produced by grassy vegetation fires versus ligneous vegetation fires following criteria of Leys et al. (2015a) and Aleman et al. (2013); d) e) and f) microcharcoal percentages of core MD96-2098 by burnt type categories using criteria of Vachula et al. (2021). b)-f) A weighted average curve using a window width of 5 was fitted to the data. Grey shaded bars indicate periods of high microcharcoal concentration.

graminoid between 2.5 and 3.5, and >3.5 for burnt graminoid. Percentages of burnt trees and (sub)shrubs, shrub/graminoid, and graminoid vegetation were then calculated.

2.3. Spectral analysis

Spectral analysis of microcharcoal concentration record (CCnb) was applied using the Lomb periodogram algorithm for unevenly sampled data (Press et al., 1992) available in the PAST software (Hammer et al., 2001), the data being linearly detrended before the analysis (Fig. 3a). In addition, to separate the time series into statistically independent components and to extract the main principal component, Singular Spectrum Analysis (SSA) was applied on the detrended CCnb record. Before SSA, data were evenly resampled at a constant 1 ka increment using the spline re-sampling function (integral-sampling procedure) of the Analyseries software (Paillard et al., 1996). The reconstructed signal is based on three principal components with a default embedding dimension parameter of 20 (Vautard and Ghil, 1989). The Multi Taper method (MTM (Thomson, 1982)) was applied on the SSA reconstruction with a bad resolution/good confidence setting (time bandwidth product = 2; number of tapers = 3) using the Analyseries software (Paillard et al., 1996) (Fig. 3b). The MTM uses harmonic analysis to estimate the total power spectrum of the time series. It is designed to estimate sharp spectral peaks in the presence of white noise (a random signal having equal intensity at different frequencies). Moreover, it also gives satisfactory results in the presence of red noise (when serially correlated in time) and it provides a high spectral resolution (Dettinger et al., 1995). The resulting spectrum has low leakage and low variance. In addition, continuous wavelet transform (Morlet wavelet (Morlet, 1983)) was applied on the detrended CCnb resampled every 1 ka by integral-sampling using a spline function (Fig. 3c).

Cross-spectral analysis between the precession index and microcharcoal concentration as well as between mean austral summer (integrated DJF months) at 25°S and microcharcoal concentration was performed using Analyseries software (Paillard et al., 1996) using a time step of 0.001370 ka, N = 366, Lags = 110, bandwidth = 0.027272 (compromise option). The timing of the strongest austral summer monsoon insolation occurs during the December 21 perihelion (precession maximum). We set the precession and the mean austral summer maximum at 0° in the phase wheel. If microcharcoal concentration plots near 0°, it means that it is coherent and in phase with the precession maximum or with the mean austral summer insolation maximum.

2.4. Climate model simulations

We explore average climate conditions and the seasonality in precipitation using the ocean-atmosphere coupled model IPSL-CM4 (Marti et al., 2010) (Fig. 4). The model includes the LMDz atmospheric model, the ORCHIDEE land surface model, the ORCA2

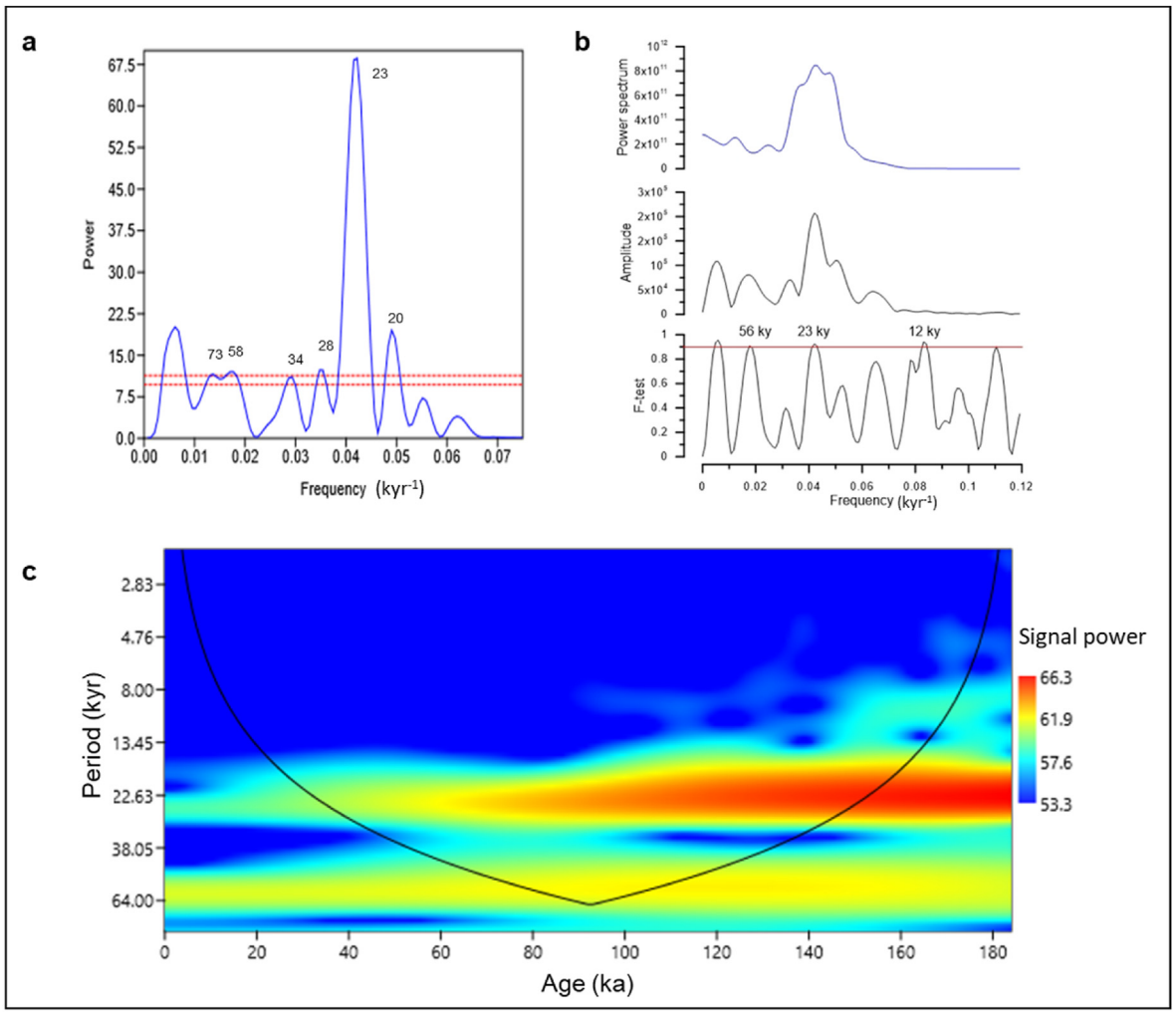

Fig. 3. Spectral analysis of CCnb. a) Lomb periodogram algorithm for unevenly sampled data available in the PAST software (Hammer et al., 2001). Red lines show the 0.01 and 0.05 significance levels; b) The Multi Taper method applied on the SSA reconstruction using the Analyseries software (Paillard et al., 1996). Red line indicates periods corresponding to significant peaks (F test >90%); c) Continuous wavelet transform (Morlet, 1983) available in the PAST software (Hammer et al., 2001) applied on the detrended CCnb resampled every 1 ka by integral-sampling using a spline function.

ocean model and the LIM2 sea-ice model. The ORCHIDEE land surface model (Krinner et al., 2005), describes natural vegetation via 11 different Plant Functional Types (PFTs). For each of those PFTs, the model computes the vegetation phenology based on climatic variables. The land fraction covered by each PFT type does not change along the simulation, however, i.e. the model is not used in dynamical vegetation mode. The IPSL-CM4 model is run with a horizontal resolution of 96 points in longitude and 71 points in latitude (3.75° × 2.53°) and 19 vertical levels for the atmosphere. The land surface model is run at the same resolution as the atmospheric model. The oceanic resolution is about 2° (0.5° near the equator) with 182 points in longitude and 149 points in latitude and 31 levels in the ocean. One simulation at 21 ka BP, the Last Glacial Maximum, was published by Kageyama et al. (2013). It included the different forcings known for this period, namely, ice sheets, greenhouse gases and insolation. Several simulations were also performed for interglacial key periods such as during the last interglacial (snapshots at 115, 122 and 126 ka BP, described in more details in Govin et al. (2012)) and the mid-Holocene (6 ka BP, described in Marzin et al. (2013)). These model simulations were forced by their corresponding insolation features (Berger, 1978b) and using the modern ice sheet configuration (Braconnot et al., 2008). The pre-industrial (PI) was set at 1850 CE (0 ka). The annual mean precipitation simulated by IPSL-CM4 over the box [15°E–35°E, 20°S-35°S] for the PI is of 1.10 mm/day (4.02 m/year). In the Global Precipitation Climatology Project observations (Huffman et al., 1997), it amounts to 1.41 mm/day or 5.16 m/year over the period 1979–2008 CE. Thus, the model underestimates this precipitation value by around 22%.

2.5. Numerical simulations of a nonlinear response on the power spectra

Nonlinear climate or proxy responses to orbital forcing result in composite frequencies in their power spectra (Laepple and Lohmann, 2009; Wigley, 1976). To investigate this effect, we generated a 200 kyr-long pseudo-precipitation time-series as linear combination of a sine wave with period of 23 kyr (like precession) and 41 kyr (like obliquity) $x(t) = k(sin(\frac{2\pi t}{23}) + 1) + (k - 1)(sin(\frac{2\pi t}{41}) + 1)$. Here, the weight k determines the relative amplitude of the 23 kyr vs. the 41 kyr cycle and is set at $k = 0.3$. As a toy model for the nonlinear response of fire (y) to precipitation (x) we choose a Gaussian response function (which can be asymmetric with a cut-off at 0) characterized by two parameters, its width σ

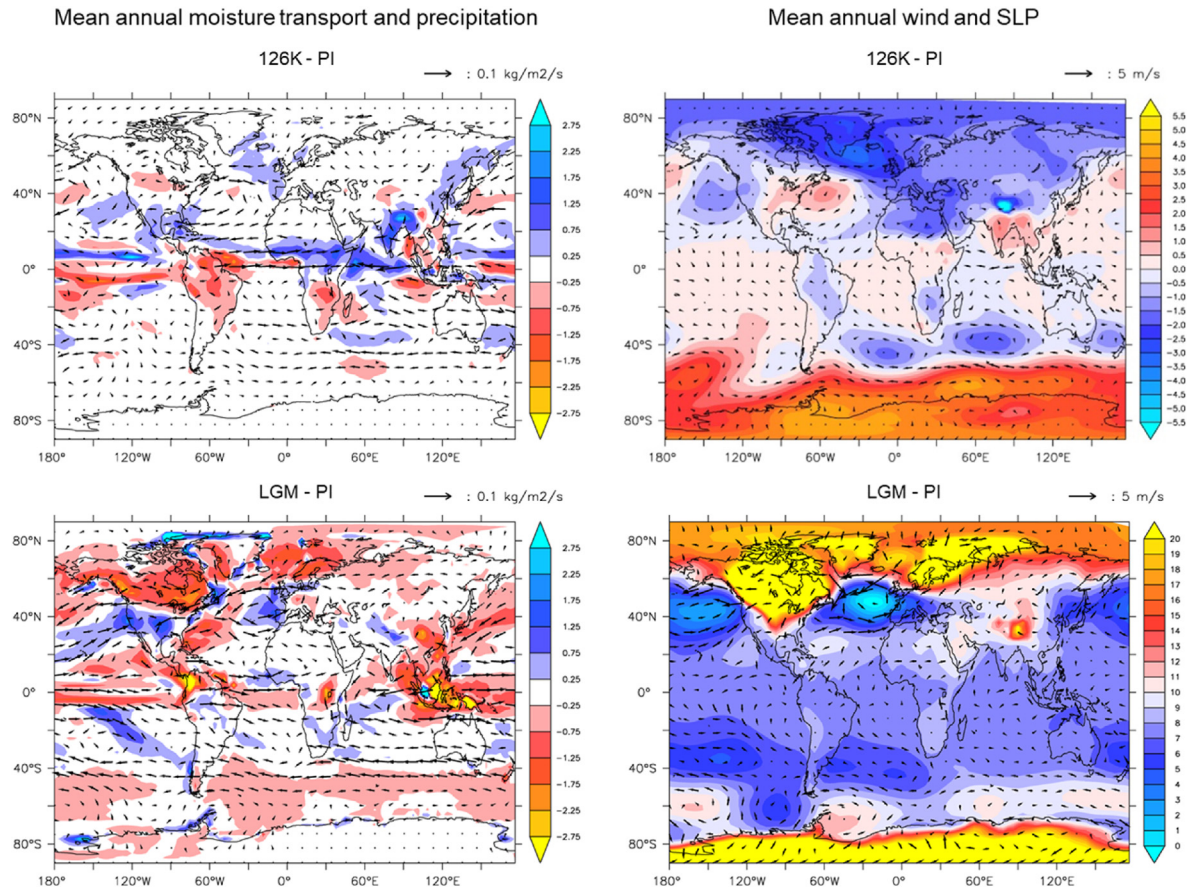

Fig. 4. Difference in annual mean climate variables simulated by the IPSL-CM4 between 126 ka and the preindustrial (PI, year 1850 CE, 0 ka) (top) and between the LGM and the PI (bottom). Left: difference in annual moisture transport (in kg/m^2/s) and precipitation (in mm/day). Right: difference between annual wind (m/s) and sea level pressure (SLP, in hPa).

and its center x_{center}.

$$y(t) = e^{-\frac{(x(t)-x_{center})^2}{2\sigma^2}}$$

As we are only interested in the relative amplitude of the different periodicities, the amplitude and phasing of the pseudo-precipitation time-series and the scaling of the toy-model response are not relevant. Spectra are analysed using a simple periodogram, but the results are independent of the spectral estimation method.

3. Results

Microcharcoal concentrations (CCnb corresponding to number of fragments per gram, and CCsurf to the total surface area per gram) are strongly positively correlated (Fig. S2, r = 0.96, p < 0.001) implying no significant fragmentation bias in using CCnb reconstruction only. CCnb shows an alternation of peaks and troughs for the last 184,000 years with maxima at approximately 20, 42, 70, 95, 115, 137, 160 and 183 ka and minima at 5, 30, 55, 83, 105, 126, 149 and 173 ka (Fig. 5a).

Charcoal influx was estimated (Fig. S4c) although core MD96-2098 presents sediment stretching in the 4.5 upper metres of the core (the last 25 ka) (Bertrand, 1996) increasing artificially the sedimentation rate in this part. It is also recognized that influx calculated by using the classic mass accumulation rates between dated sediment horizons may be overestimated due to sediment focusing in marine realm, i.e. lateral redistribution of sediment on the seafloor (Francois et al., 2004; Kienast et al., 2016; Mollenhauer et al., 2002). More accurate sedimentary fluxes in marine environment can be derived from the ^{230}Th normalization method (Francois et al., 2004), however, no measurements are available for core MD96-2098. Peaks (troughs) of microcharcoal concentrations are associated with increases (decreases) in log-transformed charcoal influx (Fig. S4c). In addition, microcharcoal concentrations display a different variability and amplitude pattern compared to marine biogenic and terrigenous material (Fig. S4a and b). These pieces of evidence suggest that neither dilution processes by marine biogenic material nor changes in river supply (high versus low river input) (Daniau et al., 2013) significantly control microcharcoal concentration fluctuations.

The charcoal marine record shows eight increases of biomass burning evenly spaced by about ~23 kyr (Fig. 5a). Peaks in biomass burning appear to be associated with maxima of the precession index (Fig. 5i) and of the mean austral summer (DJF months) insolation at the latitude of the core (25°S, Fig. 5j) (Berger, 1978b). Biomass burning shows no lag with the mean austral summer maxima (R^2 = 0.9) (not shown). In the 23 kyr band, charcoal concentration lags by 2 ± 1 kyr the precession maximum (Dec. 21 Perihelion) (R^2 = 0.9). The Lomb periodogram of CCnb (Fig. 3a) confirms the presence of significant periodicities (at 99% confidence level) in the precession-band (23 kyr) at 20, 23 and 28 ka, as well as a period at 56–58 kyr. The continuous wavelet transform approach reveals that the signal in the precession band (including the precession band at 20, 23 and 28 kyr) is particularly marked from 183 to 70 ka (Fig. 3c). It also reveals that the 56–58 kyr period detected by the Lomb periodogram over the entire time spanned by

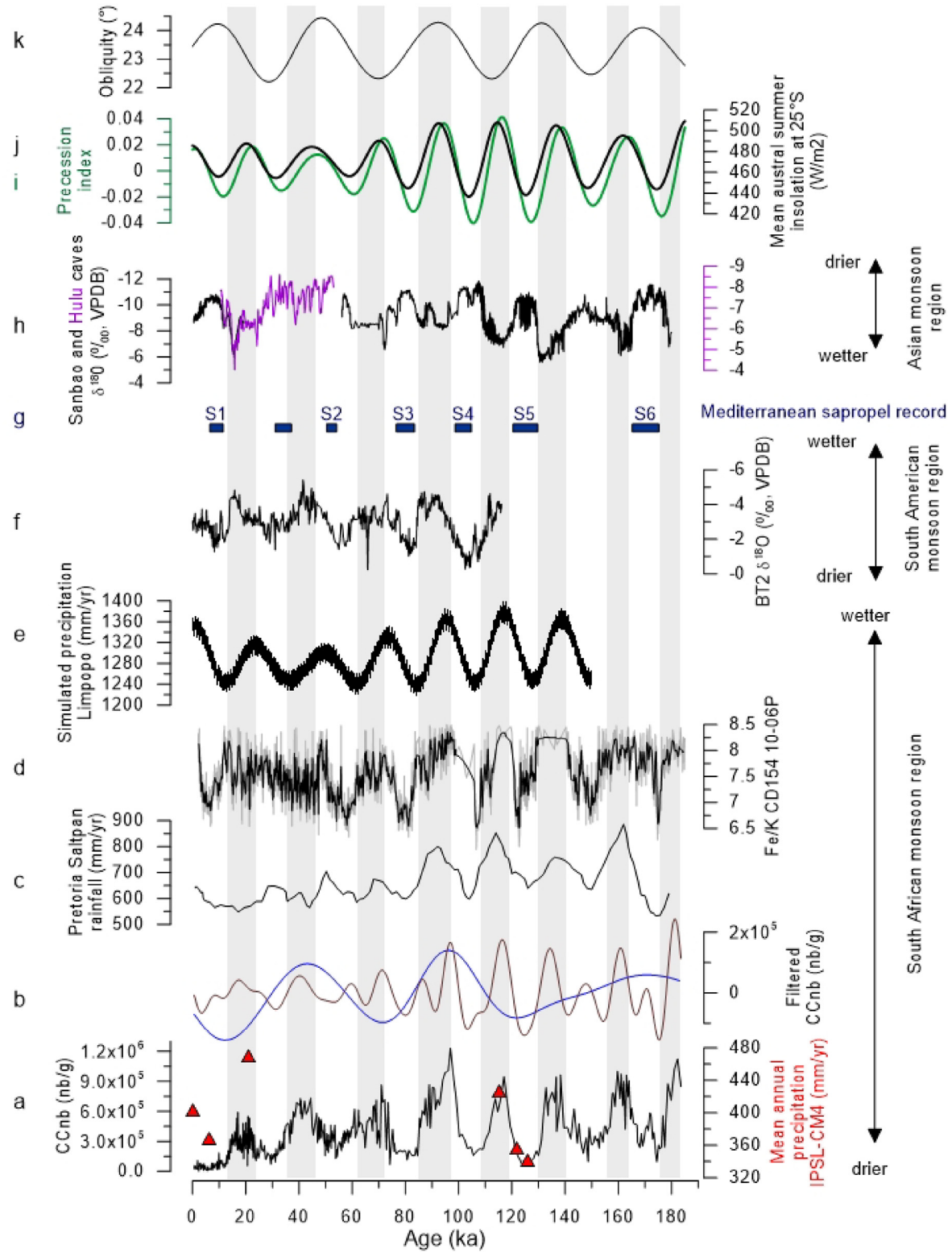

Fig. 5. Microcharcoal concentration of core MD96-2098 (this study) compared with proxies and simulation of rainfall in different monsoon domains and with orbital parameters over the past 190,000 years. a) Microcharcoal concentration of core MD96-2098 (this study) (black curve) compared to simulated mean annual precipitation for southern Africa (below 25°S) at 126, 122, 115, 21, 6 ka and PI (year 1850 CE; 0 ka) from IPSL-CM4 model (this study) (red triangles); b) Filtered components in the microcharcoal concentration obtained by Gaussian filters with the Analyseries program (Paillard et al., 1996). Band-pass filters in the 56–58 kyr band (f = 0.018 ± 0.1; blue line) and in the 12 kyr band (f = 0.08 ± 0.03 brown line) were calculated; c) the Pretorian Saltpan rainfall record (Partridge et al., 1997); d) the Fe/K ratio record of fluvial discharge of southeastern Africa (Simon et al., 2015); e) simulated precipitation in the Limpopo basin (Caley et al., 2018); f) South American monsoon record in the BT2 stalagmite at 27°S (Cruz et al., 2005); g) the sapropel records in the Mediterranean Sea (Calvert and Fontugne, 2001; Capotondi et al., 2011; Rossignol-Strick, 1985); h) Asian monsoon record from Sanbao and Hulu caves (Wang et al., 2008); i) precession index (Berger, 1978b); j) mean austral summer insolation at 25°S (Berger, 1978b); k) obliquity (Berger, 1978b). Vertical grey shaded bars indicate periods of high microcharcoal concentrations.

the MD96-2098 record have actually a band centered at 60 kyr ±8kyr (between 51 and 64 kyr) (Fig. 3c). The MTM analysis reveals three peaks centered at 56, 23 and 12 kyr in the power spectrum (significant at the 90% level) (Fig. 3b).

Microcharcoal morphology classification using different criteria (Fig. 2) suggests that particles were produced by both ligneous and grassy vegetation burning over the past 184,000 years. Peaks in microcharcoal concentration are generally associated with grassland and shrubland charcoal particles, whereas lower microcharcoal concentrations are associated with an increase in burnt ligneous (shrubs and trees) particle concentrations relative to grassland and shrubland charcoal particles.

4. Discussion

The study of Haliuc et al. (2023) suggests that concentration and morphology of microcharcoal parameters measured in marine surface sediments off Africa can be used to track fire regime on land. A high microcharcoal concentration associated with elongated particles characterise large, high intensity fires spreading through open grassland savanna (Haliuc et al., 2023).

Based on these relationships, our results suggest that large, high-intensity fires spreading through open grassland savanna dominated during precession and austral summer insolation maxima in southern Africa over the past 184 ka (Fig. 2b). At times of precession and austral insolation minima, the development of Nama-karoo (dwarf open shrubland) and of fine-leaved savanna (with a similar composition than Nama-karoo but with scattered trees) (Urrego et al., 2015) probably restricted the spread of fires, limiting charcoal production and producing less elongated particles.

Southern Africa (apart from the Fynbos Cape region) is dominated today by grass-fueled surface fires highly dependent on the amount and seasonality of rainfall controlling grass fuel availability and its flammability (Archibald et al., 2010; Brockett et al., 2001; Van Wilgen et al., 2000). In addition, C_4 grasses thrive in dry tropical savannas to the detriment of trees when rainfall intensity increases (Xu et al., 2015). In southern Africa, grass productivity increases with increased precipitation (Deshmukh, 1984; Van den Hoof et al., 2018). Zhu et al. (2016) demonstrated also experimentally that grassland Net Primary Productivity in California is highly dependent on precipitation. The atmospheric convection associated with the ITCZ is reinforced during the austral summer insolation maxima (Partridge et al., 1997) resulting in higher summer rainfall over southern Africa. In addition, increase of seasonality at precession maxima (Kutzbach et al., 2020) likely favors the drying and burning during the fire season (dry season) of the abundant grass cover that developed during the previous humid season. Finally, recurrent burning might suppress woody recruits (Bond et al., 2005). We hypothesize therefore that fire activity in southern Africa responds to changes in rainfall related to the South African monsoon variability at orbital scale.

Our fire record co-varies with rainfall estimates derived from the analysis of fine-grained sediment fraction of the Tswaing Crater record (Partridge et al., 1997) with a notable exception over the last 50 ka where peaks in fire activity appear to be associated with dry episodes in the Tswaing Crater record (Fig. 5c). This inconsistency between the two records likely results from age model uncertainties in the Tswaing Crater record. This record lacks ^{14}C dating between 31 and 7.2 radiocarbon ka, which encompasses the LGM and the early Holocene, and the age model for the 43–180 ka time interval was obtained with only two control points. Thus, contrary to what was concluded from the Tswaing Crater record (Partridge et al., 1997), our results suggest that the South African monsoon was enhanced during the 36–48 ka and 15–23 ka intervals. Interestingly, our charcoal record shows the same trend than the Tswaing crater characterized by a decrease in amplitude of precipitation peaks from about 80 ka onwards, in good accordance with the amplitude decrease of precession-related changes in insolation (Fig. 5i and j) which reflects the modulation of precession by orbital eccentricity. Our fire activity record is also in phase with the Fe/K ratio (Fig. 5d) that records fluvial discharge of southeastern Africa (Simon et al., 2015), with simulated precipitation in the Limpopo basin (Fig. 5e) (Caley et al., 2018) and with lower leaf-wax δD and higher $\delta^{13}C$ (more C4 grasses) of southwestern Africa (not shown) (Collins et al., 2014). Increased fire activity in southern Africa is contemporaneous with an intensification of the South American monsoon recorded in a stalagmite at 27°S (Fig. 5f) (Cruz et al., 2005) and anti-phased with the Asian monsoon records (Fig. 5h) (Wang et al., 2008) and the sapropel records in the Mediterranean Sea (Fig. 5g) (Calvert and Fontugne, 2001; Capotondi et al., 2011; Rossignol-Strick, 1985). Our fire record supports the idea that precession and summer insolation are the primary drivers of the South African monsoon at orbital scale.

Using the IPSL-CM4 climate model (GCM) simulations at 126, 115, 21 and 6 ka, we explored the mean annual precipitation (MAP) and its seasonality (Fig. 5b, red triangles) and the average climate conditions (only simulation maps at 126 ka and LGM are shown, Fig. 4, Fig. S3) for southern Africa (below 25°S) at times of maxima and minima in microcharcoal concentration. At 126 and 6 ka (precession minima), when our fire data suggest reduced South Africa monsoon, IPSL-CM4 climate simulations show reduced MAP relative to the preindustrial period (PI) (Fig. 5b, red triangles). This reduced MAP is chiefly driven by a decrease in austral summer precipitation (not shown) which is related to a persistent high pressure near the western tip of southern Africa (Fig. 4 and Fig. S3). This high pressure cell deviates the main wind pattern southwards and reduce the spreading of Atlantic maritime air over South East Africa. At 115 ka and during the LGM (precession maxima), when our fire data suggest enhanced South Africa monsoon, simulations show wetter annual mean conditions relative to PI in the area (Fig. 5b, red triangles; Fig. 4) associated with an increase in austral summer precipitation (not shown). Intermediate climatic conditions between 126 and 115 ka, occur at 122 ka (Fig. 5b, triangles) following well the increasing trend in microcharcoal concentration from 126 to 115 ka (Fig. 5a). Similar trend between simulated MAP and the charcoal concentration appears between the LGM, 6 ka and PI (Fig. 5b, red triangles). However, the amplitude of simulated annual rainfall is very large compared to the amplitude of charcoal signal for the LGM. Physical mechanisms behind moisture source and transport support a typical monsoonal circulation flow (Ruddiman, 2001) observed at the seasonal (not shown) and at the annual scale (Fig. 4). At 126 and 6 ka, moisture input from the Indian Ocean and associated precipitations seem to be reduced (Fig. 4), leading to dryness. At 115 ka and during the LGM, a reverse situation in the wind direction occurs and the transport in humidity flows westerly bringing precipitation from the Indian Ocean to the warmer land surface of southern Africa.

Our biomass burning record presents also a period of low amplitude centered at 58-56 kyr in the Lomb periodogram (Figs. 3a), 56 kyr in the MTM (Figs. 3b), 51–64 kyr in the wavelet analysis (Fig. 3c) as well as another one at 12 kyr while the main obliquity signal at 41 kyr is missing. A 54 kyr period was reported in the SPECMAP $\delta^{18}O$ during the Bruhnes-Matuyama transition as well as in the north Atlantic SST record of site 552 (Ruddiman et al., 1986) and in the benthic $\delta^{18}O$ record of core V19-29 located in the tropical Pacific Ocean (Berger et al., 1991). A period of 52 kyr was also observed in a terrigenous grain-size record from the northwest Arabian Sea (Clemens and Prell, 1991). The authors attributed the origin of this 52 kyr cycle in the Arabian Sea grain size to a

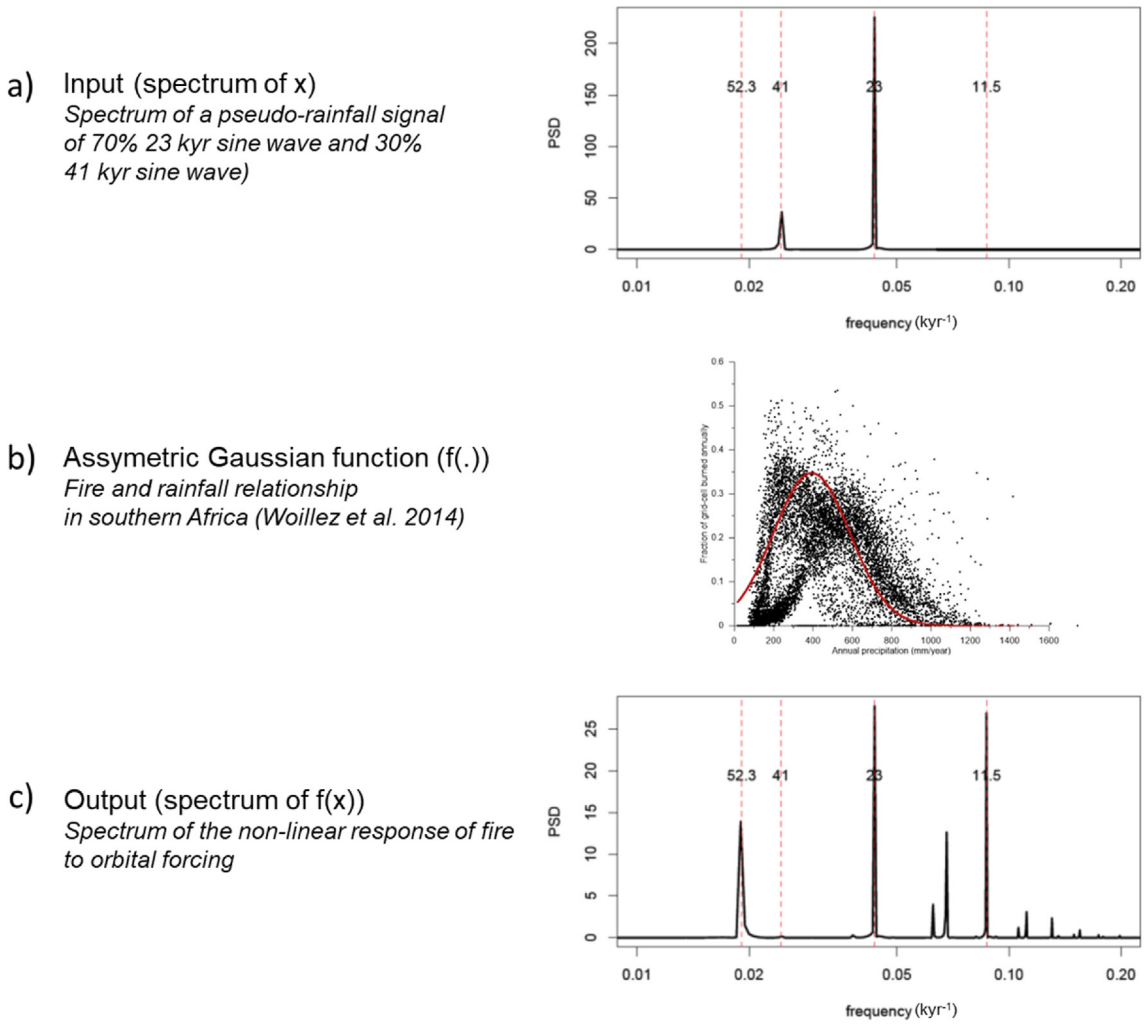

Fig. 6. Proposed scenario for the non-linear response of fire to orbital forcing (precession and obliquity) in southern Africa. a) Power spectral density (PSD) of a pseudo-rainfall signal of 70% 23 kyr sine wave and 30% 41 kyr sine wave (input). b) The pseudo-precipitation signal (a) is then transferred into a fire signal, applying an asymmetric Gaussian function representing the "intermediate rainfall" relationship using Woillez et al. (2014) as an example (the red curve is given by y = 0,34,712 × exp (-((x-392,99)^2)/(2 × 37,894), with a cut-off at 0 leading to an asymmetric distribution). c) Resulting power spectral density of the non-linear response of fire to orbital forcing.

nonlinear response of the climate system to insolation forcing at the primary Milankovitch frequency bands (41 and 23 kyr) resulting in composite frequencies (e.g. non-linear response to precession and obliquity could produce a frequency at 52 kyr^{-1} (1/23−1/41 kyr ≈1/52 kyr) (Clemens and Prell, 1991). Analysing the remaining terms in the trigonometrical expansion of precession and obliquity, Berger (1977) reported that the geological record might present, in addition to the primary period of the obliquity (41 kyr), a secondary period of 54 kyr linked also to the obliquity. In addition, a combined effect of precession and obliquity might produce two other periods of 59 and 64 kyr (Berger, 1977). The non-linear coupling of precession and obliquity could generate also combination tones at 13 and 15 kyr bands (Berger et al., 1991).

Comparing the spectral characteristic of several, long water isotope records from Asia, and using climate model simulations, Thomas et al. (2016) concluded that important spectral differences between palaeo-monsoon records from different Asian regions result from the relative influence and complex interplay between summer (oceanic) and winter (continental) monsoons recorded in the proxies. The proxy records that reflect mostly one seasonal influence (e.g. summer monsoon precipitation) tend to show simple spectra that are dominated by primary orbital frequencies and lack major heterodyne (non-primary orbital period) peaks, whereas for proxy records that are influenced by both the summer and winter monsoons, complex non-linear interactions result in the presence of heterodyne frequencies and sometimes the complete lack of primary orbital frequencies.

Based on the above elements, we make the hypothesis that the complex power spectrum observed in our palaeo-fire signal (i.e. power at 1/54, 1/23 and 1/12.9 kyr but lack of power at 1/41 kyr) stems from a nonlinear response to orbital forcing. Indeed, a non-linear response to a linear combination of precession (1/23 kyr) and obliquity (1/41 kyr) frequencies results in composite frequencies at 52 kyr period, as well as a 11.5 kyr period (a period similar to the second harmonic of the precession) (Wigley, 1976). A possible physical explanation for such a process and the occurrence of composite frequencies would be the nonlinear relationship between rainfall and fire observed between simulated present-day fraction of grid-cell burned annually and annual precipitation for southern Africa (Woillez et al., 2014) (Fig. 6b) or between the fraction of area burned and moisture availability for tropical grasslands and Mediterranean shrublands (Archibald et al., 2018).

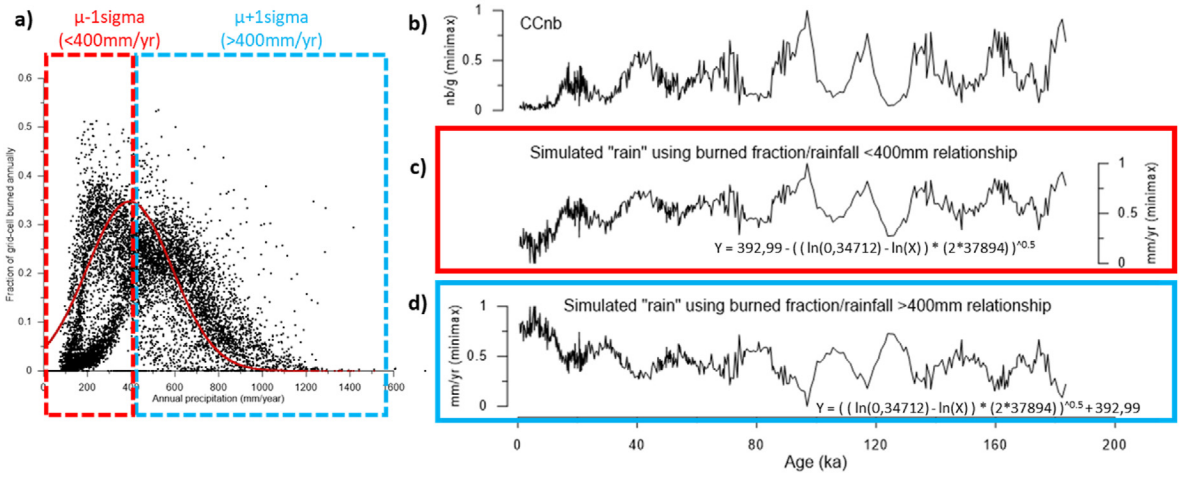

Fig. 7. a) Relationship between fraction of grid-cell burned annually and annual precipitation simulated in Woillez et al. (2014); b) microcharcoal concentration (CCnb, minimax) of core MD96-2098; c) Simulated "rain" by applying the positive relationship (a) between burned fraction and annual precipitation to the CCnb (b) using a rainfall of less than 400 mm (red rectangle) (rescaled using a minimax transformation); d) Simulated "rain" by applying the negative relationship (a) between burned fraction and annual precipitation to the CCnb (b) using a rainfall of more than 400 mm (blue rectangle) (rescaled). CCnb were rescaled to the range of the fraction of grid-cell burned annually before applying the relationship. To estimate the relationship between simulated burned fraction and annual rainfall (Woillez et al., 2014) an asymmetric Gaussian function was fitted to the data (see red curve Fig. 6b; y = 0,34,712 × exp (-((x-392,99)^2)/(2 × 37,894).

This non-linear relationship reflects the "intermediate rainfall" hypothesis observed today when a fuel-load limited ecosystem transitions to a moisture-load limited ecosystem (Archibald et al., 2018) and reconstructed in northern Africa tropical zone over the past 50 ka (Moore et al., 2022). Burned area and precipitation are positively correlated in Southern Africa, while this relationship weakens in areas located at the rainfall boundary between fuel-load/fuel moisture limited ecosystems (Alvarado et al., 2020). More rainfall leads to more fire because of increasing fuel but when too wet (even if the fuel is here) fire decreases.

The spectrum of simulated precipitation over the Limpopo basin (Caley et al., 2018) shows that the 23 and 41 kyr periods are present in the simulated precipitation (not shown), suggesting that both precession and obliquity impact the precipitation in southern Africa. The presence of a 41 kyr period in rainfall variability in the Limpopo basin remains however controversial as it is not observed in the ln (Fe/Ca) of core MD96-2098, interpreted as a proxy of rainfall (Caley et al., 2018). To back up our hypothesis of a non-linear response of fire to precipitation changes driven by a linear combination of precession and obliquity, we simulated a pseudo-precipitation signal composed of 70% 23 kyr sine wave and 30% 41 kyr sine wave (spectrum in Fig. 6a, (x)). We used this pseudo-precipitation signal to generate a fire signal by applying an asymmetric Gaussian function (Fig. 6b; (f.)) which emulates an "intermediate rainfall" relationship between precipitation and fire (based on Woillez et al. (2014)). The power spectrum of this simulated fire record (Fig. 6c; f(x)) is similar to the spectrum obtained from our charcoal data (Fig. 3). Using different combinations of the width σ and center x_{center} parameters of the Gaussian transfer function (Fig. S5) shows that this type of spectrum can only be obtained with an asymmetric Gaussian function (Fig. S5a and c). The 1/23 kyr frequency disappears when using a symmetric one (Fig. S5b and d) and the 1/52 kyr is muted when using a close to linear model (Fig. S5e).

Another possibility would be that our charcoal proxy is seasonally biased, i.e. wetter austral summers increases grass productivity while drier winters enhanced flammability. However, Ding et al. (2021) simulated dryness in both seasons during precession minima (and thus humidity in both seasons during precession maxima) with a drier summer compared to winter in southern Africa. Increased precipitation is simulated also during obliquity maxima in both seasons (Ding et al., 2021). In addition, our IPSL-CM4 results show similar precipitation levels over southern Africa during austral winters at 126 ka (precession minimum) and 115 ka (precession maximum) (not shown). We suggest therefore that composite frequencies in our record are not a result of a seasonal bias in our fire proxy and that the variability of our charcoal record results from a non-linear response of fire to a linear combination of precession and obliquity forcings.

This scenario is in line with different modeling results which show that the African summer monsoon is influenced both by precession and obliquity (Bosmans et al., 2015a, 2015b; Tuenter et al., 2003) with increased rainfall in southern Africa during precession (Simon et al., 2015) and obliquity maxima (Ding et al., 2021). With such orbital configurations, increased rainfall results either from stronger easterly surface winds blowing over southern Africa and an increased land convection during precession maxima (Simon et al., 2015) or from a stronger cross-equatorial moisture transport into the summer hemisphere during high obliquity maxima (Bosmans et al., 2015b; Ding et al., 2021). Woillez et al. (2014) conducted simulations which show increases in the fraction of grid-cell burned annually for precipitation ranges between 0 and 300 mm/yr or between 0 and 600 mm/yr (Fig. 4a, red dashed-line rectangles), and decreases for precipitation >400 mm or >600 mm/yr (Fig. 4a, blue dashed-line rectangles). These patterns in the burned fraction reflect the simulated grass fractions which globally increase with annual precipitation with two peaks around annual precipitation values of 300 and 600 mm. yr^{-1}. The first one corresponds to the hinterland of the Cape region where precipitation occurs during the austral winter and the second one reflects the gradual increase and decrease of grass fractions from the west to the east of southern Africa associated with the austral summer rainfall gradient (Woillez et al., 2014). As precipitation increased in both seasons during precession or obliquity maxima, a seasonal bias in our fire proxy coming from seasonal grass productivity is not expected either.

We simulated rainfall variability using our charcoal record, rescaling our charcoal data to the range of the fraction of grid-cell burned annually and by applying the relationships μ-1sigma (positive relationship) and μ+1sigma (negative relationship) (μ

corresponding to the mean annual precipitation, here set at 400 mm for an example between the two peaks of precipitation at 300 or 600 mm/year, Fig. 7a). Rainfall variability is in phase with our charcoal record when using the *burned* fraction/rainfall below 400 mm/year relationship (Fig. 7c). When using *burned fraction/rainfall ab*ove 400 mm/yr relationship, rainfall variability is opposite to the charcoal record (Fig. 7d). This suggests that charcoal peaks reflect dry periods. We suggest therefore that the annual range of precipitation in southern Africa lies in the lower range (0–300 or 0–600 mm/yr) over the past 184,000 years. This result is consistent with the glacial/interglacial range of annual rainfall over southern Africa (300–500 mm/year) simulated over key periods using the IPSL-CM4 (Fig. 5b).

5. Conclusion

In summary, there were eight cycles of increased burning of open-grassland savanna in southern Africa over the past 184,00 years, which corresponds to an average frequency of about 23 kyr. Thus, these eight peaks likely reflects the enhancement of monsoon-related rainfall in southern Africa, in response to precession-driven austral summer insolation changes. In addition, two non-primary orbital periodicities are observed in the charcoal record at 56–58 kyr and 12 kyr. They likely reflect a non-linear response of fire to a linear combination of precession (1/23 kyr) and obliquity (1/41 kyr) frequencies, which would be embedded in the rainfall and the South African monsoon variability. The non-linear response of fire to rainfall lies in the "intermediate rainfall" hypothesis represented by an asymmetric Gaussian relationship between fire and precipitation. This exercise results in frequencies of 1/23, 1/54 and 1/12 kyr in the simulated charcoal record with no primary obliquity frequency. In addition to the precession-driven global monsoon concept, our charcoal record supports the idea that obliquity plays an additional role in modulating the South African monsoon at latitudes higher than 25°S.

Author contributions

A.-L.D designed the study, performed charcoal measurements, analysed results and led the interpretation and the manuscript writing. M.-F.L. and H.C. advised on spectral analyses and data pretreatment. D. S and M.K. performed climate simulations. D.S. derived exponential relationship of Fig. 4. T.L contributed to the interpretation of the non-linear orbital response and performed mathematical demonstration of Fig. S5. B.M. and K.C performed isotope analysis on Melonis barleanum. All authors commented on the manuscript.

Declaration of competing interest

The authors declare that they have no known competing financial interests or personal relationships that could have appeared to influence the work reported in this paper.

Data availability

The data generated and analysed during the current study are available at https://doi.org/10.6084/m9.figshare.22787285 and at https://doi.org/10.6084/m9.figshare.22787294.

Acknowledgements

This research was supported by the ANR BRAISE project, grant ANR-19-CE01-0001-01 of the French Agence Nationale de la Recherche; French INSU (Institut National des Sciences de l'Univers) programme LEFE (Les Enveloppes Fluides et l'Environnement) CAMPFIRE project; by the European Research Council (ERC) Advanced Grant TRACSYMBOLS 249587 and by the project PICS CNRS 06484. T.L. was supported by the ERC under the European Union's Horizon 2020 research and innovation programme (grant agreement no. 716092). The IPSLCM4 simulations were run on TGCC (Très Grand Center de Calcul du CEA) supercomputers via a GENCI (Grand Equipement National de Calcul Intensif) allocation gen2212. TGCC and GENCI are both acknowledged for having made the simulations possible. We warmly thank P. Braconnot for providing IPSL-CM4 simulation at 126 ka, M. Georget for microcharcoal slide preparation, L. Rossignol and M.-H. Castéra for *Melonis barleanum* foraminifera picking.

We thank Margit Simon and an anonymous reviewer for their valuable comments.

Appendix A. Supplementary data

Supplementary data related to this article can be found at https://doi.org/10.1016/j.quascirev.2023.108128.

References

Aleman, J.C., Blarquez, O., Bentaleb, I., Bonté, P., Brossier, B., Carcaillet, C., Gond, V., Gourlet-Fleury, S., Kpolita, A., Lefèvre, I., Oslisly, R., Power, M.J., Yongo, O., Bremond, L., Favier, C., 2013. Tracking land-cover changes with sedimentary charcoal in the Afrotropics. Holocene 23, 1853–1862.

Archibald, S., Lehmann, C.E.R., Belcher, C.M., Bond, W.J., Bradstock, R.A., Daniau, A.L., Dexter, K.G., Forrestel, E.J., Greve, M., He, T., Higgins, S.I., Hoffmann, W.A., Lamont, B.B., McGlinn, D.J., Moncrieff, G.R., Osborne, C.P., Pausas, J.G., Price, O., Ripley, B.S., Rogers, B.M., Schwilk, D.W., Simon, M.F., Turetsky, M.R., Van der Werf, G.R., Zanne, A.E., 2018. Biological and geophysical feedbacks with fire in the Earth system. Environ. Res. Lett. 13, 033003.

Archibald, S., Scholes, R.J., Roy, D.P., Roberts, G., Boschetti, L., 2010. Southern African fire regimes as revealed by remote sensing. Int. J. Wildland Fire 19, 861–878.

Berger, A., 1978a. Long-term variations of daily insolation and Quaternary climatic changes. J. Atmos. Sci. 35, 2362–2367.

Berger, A., Melice, J.L., Hinnov, L., 1991. A strategy for frequency spectra of quaternary climate records. Clim. Dynam. 5, 227–240.

Berger, A.L., 1977. Support for the astronomical theory of climatic change. Nature 269, 44–45.

Berger, A.L., 1978b. Long-term variations of daily insolation and quaternary climatic changes. J. Atmos. Sci. 35, 2362–2367.

Bertrand, P., 1996. NAUSICAA-IMAGES 2-MD105 Cruise. RV Marion Dufresne.

Blaauw, M., 2010. Methods and code for 'classical' age-modelling of radiocarbon sequences. Quat. Geochronol. 5, 512–518.

Bond, W.J., Woodward, F.I., Midgley, G.F., 2005. The global distribution of ecosystems in a world without fire. New Phytol. 165, 525–538.

Bosmans, J.H.C., Drijfhout, S.S., Tuenter, E., Hilgen, F.J., Lourens, L.J., 2015a. Response of the North African summer monsoon to precession and obliquity forcings in the EC-Earth GCM. Clim. Dynam. 44, 279–297.

Bosmans, J.H.C., Hilgen, F.J., Tuenter, E., Lourens, L.J., 2015b. Obliquity forcing of low-latitude climate. Clim. Past 11, 1335–1346.

Braconnot, P., Marzin, C., Grégoire, L., Mosquet, E., Marti, O., 2008. Monsoon response to changes in Earth's orbital parameters: comparisons between simulations of the Eemian and of the Holocene. Clim. Past 4, 281–294.

Braun, K., Bar-Matthews, M., Matthews, A., Ayalon, A., Cowling, R.M., Karkanas, P., Fisher, E.C., Dyez, K., Zilberman, T., Marean, C.W., 2018. Late Pleistocene records of speleothem stable isotopic compositions from Pinnacle Point on the South African south coast. Quat. Res. 91, 265–288.

Brockett, B.H., Biggs, H.C., van Wilgen, B.W., 2001. A patch mosaic burning system for conservation areas in southern African savannas. Int. J. Wildland Fire 10, 169–183.

Burns, S.J., McGee, D., Scroxton, N., Kinsley, C.W., Godfrey, L.R., Faina, P., Ranivoharimanana, L., 2022. Southern Hemisphere controls on ITCZ variability in southwest Madagascar over the past 117,000 years. Quat. Sci. Rev. 276, 107317.

Caley, T., Extier, T., Collins, J.A., Schefuß, E., Dupont, L., Malaizé, B., Rossignol, L., Souron, A., McClymont, E.L., Jimenez-Espejo, F.J., García-Comas, C., Eynaud, F., Martinez, P., Roche, D.M., Jorry, S.J., Charlier, K., Wary, M., Gourves, P.-Y., Billy, I., Giraudeau, J., 2018. A two-million-year-long hydroclimatic context for hominin evolution in southeastern Africa. Nature 560, 76–79.

Caley, T., Kim, J.H., Malaizé, B., Giraudeau, J., Laepple, T., Caillon, N., Charlier, K., Rebaubier, H., Rossignol, L., Castañeda, I.S., Schouten, S., Sinninghe Damsté, J.S., 2011a. High-latitude obliquity as a dominant forcing in the Agulhas current system. Clim. Past 7, 1285–1296.

Caley, T., Malaizé, B., Revel, M., Ducassou, E., Wainer, K., Ibrahim, M., Shoeaib, D., Migeon, S., Marieu, V., 2011b. Orbital timing of the Indian, East Asian and

African boreal monsoons and the concept of a 'global monsoon. Quat. Sci. Rev. 30, 3705–3715.
Caley, T., Malaizé, B., Zaragosi, S., Rossignol, L., Bourget, J., Eynaud, F., Martinez, P., Giraudeau, J., Charlier, K., Ellouz-Zimmermann, N., 2011c. New Arabian Sea records help decipher orbital timing of Indo-Asian monsoon. Earth Planet Sci. Lett. 308, 433–444.
Calvert, S.E., Fontugne, M.R., 2001. On the late Pleistocene-Holocene sapropel record of climatic and oceanographic variability in the eastern Mediterranean. Paleoceanography 16, 78–94.
Capotondi, L., Vigliotti, L., Bergami, C., Sangiorgi, F., 2011. The Dark Side of the Mediterranean Geological Record: the Sapropel Layers and a Case Study from the Ionian Sea, pp. 658–669.
Chase, B., Harris, C., de Wit, M.J., Kramers, J., Doel, S., Stankiewicz, J., 2021. South African speleothems reveal influence of high- and low-latitude forcing over the past 113.5 k. y. Geology 49, 1353–1357.
Cheng, H., Sinha, A., Wang, X., Cruz, F.W., Edwards, R.L., 2012. The global paleomonsoon as seen through speleothem records from Asia and the americas. Clim. Dynam. 39, 1045–1062.
Clemens, S., Prell, W., 1991. One million year record of summer monsoon winds and continental aridity from the Owen Ridge (Site 722), northwest Arabian Sea. In: Prell, W.N.N., et al. (Eds.), Proceedings of the Ocean Drilling Program, Scientific Results. Ocean Drilling Program), College Station, TX, pp. 365–388.
Clemens, S.C., Prell, W.L., 1990. Late Pleistocene variability of Arabian Sea summer monsoon winds and continental aridity: eolian records from the lithogenic component of deep-sea sediments. Paleoceanography 5, 109–145.
Clemens, S.C., Prell, W.L., 2003. A 350,000 year summer-monsoon multi-proxy stack from the owen ridge, northern Arabian Sea. Mar. Geol. 201, 35–51.
Collins, J.A., Schefuß, E., Govin, A., Mulitza, S., Tiedemann, R., 2014. Insolation and glacial–interglacial control on southwestern African hydroclimate over the past 140 000 years. Earth Planet Sci. Lett. 398, 1–10.
Crocker, A.J., Naafs, B.D.A., Westerhold, T., James, R.H., Cooper, M.J., Röhl, U., Pancost, R.D., Xuan, C., Osborne, C.P., Beerling, D.J., Wilson, P.A., 2022. Astronomically controlled aridity in the Sahara since at least 11 million years ago. Nat. Geosci. 15, 671–676.
Cruz, F.W., Burns, S.J., Karmann, I., Sharp, W.D., Vuille, M., Cardoso, A.O., Ferrari, J.A., Silva Dias, P.L., Viana, O., 2005. Insolation-driven changes in atmospheric circulation over the past 116,000 years in subtropical Brazil. Nature 434, 63–66.
Daniau, A.-L., Sánchez Goñi, M.F., Martinez, P., Urrego, D.H., Bout-Roumazeilles, V., Desprat, S., Marlon, J.R., 2013. Orbital-scale climate forcing of grassland burning in southern Africa. Proc. Natl. Acad. Sci. USA 110, 5069–5073.
deMenocal, P.B., 1995. Plio-pleistocene african climate. Science 270, 53–59.
Deshmukh, I.K., 1984. A common relationship between precipitation and grassland peak biomass for East and southern Africa. Afr. J. Ecol. 22, 181–186.
Dettinger, M.D., Ghil, M., Strong, C.M., Weibel, W., Yiou, P., 1995. Software expedites singular-spectrum analysis of noisy time series. Eos, Transactions American Geophysical Union 76, 12–21.
Ding, Z., Huang, G., Liu, F., Wu, R., Wang, P., 2021. Responses of global monsoon and seasonal cycle of precipitation to precession and obliquity forcing. Clim. Dynam. 56, 3733–3747.
Drysdale, R.N., Zanchetta, G., Hellstrom, J.C., Fallick, A.E., McDonald, J., Cartwright, I., 2007. Stalagmite evidence for the precise timing of North Atlantic cold events during the early last glacial. Geology 35, 77–80.
Dupont, L., 2011. Orbital scale vegetation change in Africa. Quat. Sci. Rev. 30, 3589–3602.
Dupont, L.M., Caley, T., Kim, J.H., Castañeda, I., Malaizé, B., Giraudeau, J., 2011. Glacial-interglacial vegetation dynamics in South Eastern Africa coupled to sea surface temperature variations in the Western Indian Ocean. Clim. Past 7, 1209–1224.
Dupont, L.M., Zhao, X., Charles, C., Faith, J.T., Braun, D., 2022. Continuous vegetation record of the greater Cape floristic region (South Africa) covering the past 300000 years (IODP U1479). Clim. Past 18, 1–21.
Francois, R., Frank, M., Rutgers van der Loeff, M.M., Bacon, M.P., 2004. 230Th normalization: an essential tool for interpreting sedimentary fluxes during the late Quaternary. Paleoceanography 19, PA1018.
Gouzy, A., Malaizé, B., Pujol, C., Charlier, K., 2004. Climatic "pause" during Termination II identified in shallow and intermediate waters off the Iberian margin. Quat. Sci. Rev. 23, 1523–1528.
Govin, A., Braconnot, P., Capron, E., Cortijo, E., Duplessy, J.C., Jansen, E., Labeyrie, L., Landais, A., Marti, O., Michel, E., Mosquet, E., Risebrobakken, B., Swingedouw, D., Waelbroeck, C., 2012. Persistent influence of ice sheet melting on high northern latitude climate during the early Last Interglacial. Clim. Past 8, 483–507.
Graham, D.W., Corliss, B.H., Bender, M.L., Keigwin, L.D., 1981. Carbon and oxygen isotopic disequilibria of recent deep-sea benthic foraminifera. Mar. Micropaleontol. 6, 483–497.
Haliuc, A., Daniau, A.-L., Mouillot, F., Chen, W., Leys, B., David, V., Hanquiez, V., Dennielou, B., Schefuß, E., Bayon, G., Crosta, X., 2023. Microscopic charcoals in ocean sediments off Africa track past fire intensity from the continent. Communications Earth & Environment 4, 1–11.
Hammer, Ø., Harper, D.A.T., Ryan, P.D., 2001. Past: paleontological statistics software package for education and data analysis. Palaeontol. Electron. 4, 1–9.
Heaton, T.J., Köhler, P., Butzin, M., Bard, E., Reimer, R.W., Austin, W.E.N., Bronk Ramsey, C., Grootes, P.M., Hughen, K.A., Kromer, B., Reimer, P.J., Adkins, J., Burke, A., Cook, M.S., Olsen, J., Skinner, L.C., 2020. Marine20—the marine radiocarbon age calibration curve (0–55,000 cal BP). Radiocarbon 62, 779–820.
Henderson, G.M., Slowey, N.C., 2000. Evidence from U-Th dating against Northern Hemisphere forcing of the penultimate deglaciation. Nature 404, 61–66.
Huffman, G.J., Adler, R.F., Arkin, P., Chang, A., Ferraro, R., Gruber, A., Janowiak, J., McNab, A., Rudolf, B., Schneider, U., 1997. The global precipitation Climatology project (GPCP) combined precipitation dataset. Bull. Am. Meteorol. Soc. 78, 5–20.
Jones, T.P., Chaloner, W.G., Kuhlbusch, T.A.J., 1997. Proposed bio-geological and chemical based terminology for fire-altered plant matter. In: Clark, J.S., Cachier, H., Goldammer, J.G., Stocks, B. (Eds.), Sediment Records of Biomass Burning and Global Change. Springer-Verlag Berlin Heidelberg, pp. 9–22.
Kageyama, M., Braconnot, P., Bopp, L., Caubel, A., Foujols, M.-A., Guilyardi, E., Khodri, M., Lloyd, J., Lombard, F., Mariotti, V., Marti, O., Roy, T., Woillez, M.-N., 2013. Mid-Holocene and Last Glacial Maximum climate simulations with the IPSL model—part I: comparing IPSL_CM5A to IPSL_CM4. Clim. Dynam. 40, 2447–2468.
Kienast, S.S., Winckler, G., Lippold, J., Albani, S., Mahowald, N.M., 2016. Tracing dust input to the global ocean using thorium isotopes in marine sediments: ThoroMap. Global Biogeochem. Cycles 30, 1526–1541.
Krinner, G., Viovy, N., de Noblet-Ducoudré, N., Ogée, J., Polcher, J., Friedlingstein, P., Ciais, P., Sitch, S., Prentice, I.C., 2005. A dynamic global vegetation model for studies of the coupled atmosphere-biosphere system. Global Biogeochem. Cycles 19, GB1015.
Kutzbach, J.E., Guan, J., He, F., Cohen, A.S., Orland, I.J., Chen, G., 2020. African climate response to orbital and glacial forcing in 140,000-y simulation with implications for early modern human environments. Proc. Natl. Acad. Sci. USA 117, 2255–2264.
Kutzbach, J.E., Liu, X., Liu, Z., Chen, G., 2008. Simulation of the evolutionary response of global summer monsoons to orbital forcing over the past 280,000 years. Clim. Dynam. 30, 567–579.
Laepple, T., Lohmann, G., 2009. Seasonal cycle as template for climate variability on astronomical timescales. Paleoceanography 24, PA4201.
Leys, B., Brewer, S.C., McConaghy, S., Mueller, J., McLauchlan, K.K., 2015. Fire history reconstruction in grassland ecosystems: amount of charcoal reflects local area burned. Environ. Res. Lett. 10, 114009.
Leys, B., Carcaillet, C., Dezileau, L., Ali, A.A., Bradshaw, R.H.W., 2013. A comparison of charcoal measurements for reconstruction of Mediterranean paleo-fire frequency in the mountains of Corsica. Quat. Res. 79, 337–349.
Lisiecki, L., Raymo, M.E., 2005. A Pliocene-Pleistocene stack of 57 globally distributed benthic δ 18 O records. Paleoceanography 20, PA1003.
Marti, O., Braconnot, P., Dufresne, J.L., Bellier, J., Benshila, R., Bony, S., Brockmann, P., Cadule, P., Caubel, A., Codron, F., de Noblet, N., Denvil, S., Fairhead, L., Fichefet, T., Foujols, M.A., Friedlingstein, P., Goosse, H., Grandpeix, J.Y., Guilyardi, E., Hourdin, F., Idelkadi, A., Kageyama, M., Krinner, G., Lévy, C., Madec, G., Mignot, J., Musat, I., Swingedouw, D., Talandier, C., 2010. Key features of the IPSL ocean atmosphere model and its sensitivity to atmospheric resolution. Clim. Dynam. 34, 1–26.
Marzin, C., Kallel, N., Kageyama, M., Duplessy, J.C., Braconnot, P., 2013. Glacial fluctuations of the Indian monsoon and their relationship with North Atlantic climate: new data and modelling experiments. Clim. Past 9, 2135–2151.
Masson-Delmotte, V., Stenni, B., Pol, K., Braconnot, P., Cattani, O., Falourd, S., Kageyama, M., Jouzel, J., Landais, A., Minster, B., Barnola, J.M., Chappellaz, J., Krinner, G., Johnsen, S., Röthlisberger, R., Hansen, J., Mikolajewicz, U., Otto-Bliesner, B., 2010. EPICA Dome C record of glacial and interglacial intensities. Quat. Sci. Rev. 29, 113–128.
McIntyre, A., Ruddiman, W.F., Karlin, K., Mix, A.C., 1989. Surface water response of the equatorial Atlantic Ocean to orbital forcing. Paleoceanography 4, 19–55.
Mollenhauer, G., Schneider, R.R., Müller, P.J., Spieß, V., Wefer, G., 2002. Glacial/interglacial variablity in the Benguela upwelling system: spatial distribution and budgets of organic carbon accumulation. Global Biogeochem. Cycles 16, 1134.
Mooney, S., Tinner, W., 2011. The analysis of charcoal in peat and organic sediments. Mires Peat 7, 1–18.
Moore, H.R., Crocker, A.J., Belcher, C.M., Meckler, A.N., Osborne, C.P., Beerling, D.J., Wilson, P.A., 2022. Hydroclimate variability was the main control on fire activity in northern Africa over the last 50,000 years. Quat. Sci. Rev. 288, 107578.
Morlet, J., 1983. Sampling theory and wave propagation. In: Chen, C.H. (Ed.), Issues in Acoustic Signal — Image Processing and Recognition. Springer Berlin Heidelberg, Berlin, Heidelberg, pp. 233–261.
Müller, P.J., 2003. Density and Water Content of Sediment Core GeoB1711-4. Department of Geosciences, PANGAEA. https://doi.org/10.1594/PANGAEA.96479.
Paillard, D., Labeyrie, L., Yiou, P., 1996. Macintosh Program performs time-series analysis. Eos, Transactions American Geophysical Union 77, 379-379.
Partridge, T.C., 1997. Cainozoic environmental change in southern Africa, with special emphasis on the last 200 000 years. Prog. Phys. Geogr. Earth Environ. 21, 3–22.
Partridge, T.C., Demenocal, P.B., Lorentz, S.A., Paiker, M.J., Vogel, J.C., 1997. Orbital forcing of climate over South Africa: a 200,000-year rainfall record from the Pretoria Saltpan. Quat. Sci. Rev. 16, 1125–1133.
Patterson, W.A.I., Edwards, K.J., Maguire, D.J., 1987. Microscopic charcoal as a fossil indicator of fire. Quat. Sci. Rev. 6, 3–23.
Pichevin, L., Martinez, P., Bertrand, P., Schneider, R., Giraudeau, J., Emeis, K., 2005. Nitrogen cycling on the Namibian shelf and slope over the last two climatic cycles: local and global forcings. Paleoceanography 20, PA2006.
Press, W.H., Teukolsky, S.A., Vetterling, W.T., Flannery, B.P., 1992. Numerical Recipes

in C, second ed. Cambridge University Press.
Rossignol-Strick, M., 1985. Mediterranean Quaternary sapropels, an immediate response of the African monsoon to variation of insolation. Palaeogeogr. Palaeoclimatol. Palaeoecol. 49, 237–263.
Ruddiman, W.F., 2001. Earth's Climate: Past and Future. W.H. Freeman & Sons, New York.
Ruddiman, W.F., Shackleton, N.J., McIntyre, A., 1986. North Atlantic sea-surface temperatures for the last 1.1 million years. Geological Society, London, Special Publications 21, 155–173.
Sanchez Goñi, M.F., Harrison, S., 2010. Millennial-scale climate variability and vegetation changes during the Last Glacial: concepts and terminology. Quat. Sci. Rev. 29, 2823–2827.
Simon, M.H., Ziegler, M., Bosmans, J., Barker, S., Reason, C.J.C., Hall, I.R., 2015. Eastern South African hydroclimate over the past 270,000 years. Sci. Rep. 5, 18153.
Skonieczny, C., McGee, D., Winckler, G., Bory, A., Bradtmiller, L.I., Kinsley, C.W., Polissar, P.J., De Pol-Holz, R., Rossignol, L., Malaizé, B., 2019. Monsoon-driven Saharan dust variability over the past 240,000 years. Sci. Adv. 5, eaav1887.
Stuiver, M., Reimer, P.J., 1993. CALIB rev. 8. Radiocarbon 35, 215–230.
Thomas, E.K., Clemens, S.C., Sun, Y., Prell, W.L., Huang, Y., Gao, L., Loomis, S., Chen, G., Liu, Z., 2016. Heterodynes dominate precipitation isotopes in the East Asian monsoon region, reflecting interaction of multiple climate factors. Earth Planet Sci. Lett. 455, 196–206.
Thomson, D.J., 1982. Spectrum estimation and harmonic analysis. IEEE Proc 70, 1055–1096.
Tiedemann, R., Sarnthein, M., Shackleton, N.J., 1994. Astronomic timescale for the pliocene atlantic δ18O and dust flux records of ocean drilling program site 659. Paleoceanography 9, 619–638.
Tsakiridou, M., Cunningham, L., Hardiman, M., 2020. Toward a standardized procedure for charcoal analysis. Quat. Res. 99, 329–340.
Tuenter, E., Weber, S.L., Hilgen, F.J., Lourens, L.J., 2003. The response of the African summer monsoon to remote and local forcing due to precession and obliquity. Global Planet. Change 36, 219–235.
Urrego, D.H., Sánchez Goñi, M.F., Daniau, A.L., Lechevrel, S., Hanquiez, V., 2015. Increased aridity in southwestern Africa during the warmest periods of the last interglacial. Clim. Past 11, 1417–1431.
Vachula, R.S., Sae-Lim, J., Li, R., 2021. A critical appraisal of charcoal morphometry as a paleofire fuel type proxy. Quat. Sci. Rev. 262, 106979.
Van den Hoof, C., Verstraete, M., Scholes, R.J., 2018. Differing responses to rainfall suggest more than one functional type of grassland in South Africa. Rem. Sens. 10, 2055.
Van Wilgen, B.W., Biggs, H., O'Regan, S.P., Mare, N., 2000. Fire history of the savanna ecosystems in the kruger national park, South Africa, between 1941 and 1996. South Afr. J. Sci. 96, 167–178.
Vautard, R., Ghil, M., 1989. Singular spectrum analysis in nonlinear dynamics, with applications to paleoclimatic time series. Phys. Nonlinear Phenom. 35, 395–424.
Waelbroeck, C., Frank, N., Jouzel, J., Parrenin, F., Masson-Delmotte, V., Genty, D., 2008. Transferring radiometric dating of the last interglacial sea level high stand to marine and ice core records. Earth Planet Sci. Lett. 265, 183–194.
Wang, P., 2009. Global monsoon in a geological perspective. Chin. Sci. Bull. 54, 1113–1136.
Wang, P.X., Wang, B., Cheng, H., Fasullo, J., Guo, Z., Kiefer, T., Liu, Z., 2017. The global monsoon across time scales: mechanisms and outstanding issues. Earth Sci. Rev. 174, 84–121.
Wang, P.X., Wang, B., Cheng, H., Fasullo, J., Guo, Z.T., Kiefer, T., Liu, Z.Y., 2014. The global monsoon across timescales: coherent variability of regional monsoons. Clim. Past 10, 2007–2052.
Wang, Y., Cheng, H., Edwards, R.L., Kong, X., Shao, X., Chen, S., Wu, J., Jiang, X., Wang, X., An, Z., 2008. Millennial- and orbital-scale changes in the East Asian monsoon over the past 224,000 years. Nature 451, 1090–1093.
Whitlock, C., Larsen, C., 2001. Charcoal as a fire proxy. In: Smol, J.P., Birks, H.J.B., Last, W.M. (Eds.), Tracking Environmental Changes Using Lake Sediments. Kluwer Academic Publishers, Dordrecht, The Netherlands, pp. 75–96.
Wigley, T.M.L., 1976. Spectral analysis and the astronomical theory of climatic change. Nature 264, 629–631.
Woillez, M.N., Levavasseur, G., Daniau, A.L., Kageyama, M., Urrego, D.H., Sánchez-Goñi, M.F., Hanquiez, V., 2014. Impact of precession on the climate, vegetation and fire activity in southern Africa during MIS4. Clim. Past 10, 1165–1182.
Xu, X., Medvigy, D., Rodriguez-Iturbe, I., 2015. Relation between rainfall intensity and savanna tree abundance explained by water use strategies. Proc. Natl. Acad. Sci. USA 112, 12992–12996.
Zhu, K., Chiariello, N.R., Tobeck, T., Fukami, T., Field, C.B., 2016. Nonlinear, interacting responses to climate limit grassland production under global change. Proc. Natl. Acad. Sci. USA 113, 10589–10594.